Topographic Blocking in Flows with Non-Uniform Upstream Static-Stability Profiles

Patrick Alexander Reinecke

A thesis submitted in partial fulfillment
of the requirements for the degree of

Master of Science

University of Washington

2005

Program Authorized to Offer Degree: Atmospheric Sciences

University of Washington

Graduate School

This is to certify that I have examined this copy of a master's thesis by

Patrick Alexander Reinecke

and have found that it is complete and satisfactory in all respects,
and that any and all revisions required by the final
examining committee have been made.

Committee Members:

_____

Dale R. Durran

_____

Clifford F. Mass

_____

Christopher S. Bretherton

Date: _____

In presenting this thesis in partial fulfillment of the requirements for a master's degree at the University of Washington, I agree that the Library shall make its copies freely available for inspection. I further agree that extensive copying of this thesis is allowable only for scholarly purposes, consistent with "fair use" as prescribed in the U.S. Copyright Law. Any other reproduction for any purpose or by any means shall not be allowed without my written permission.

Signature_____

Date_____

TABLE OF CONTENTS

LIST OF FIGURES

Chapter 1

INTRODUCTION

The ability to determine if flow impinging a mountain rises over the mountain freely or is blocked and deviates around the mountain is of great practical importance in regions of complex terrain. In addition to the impact on pollution dispersion, barrier and flank jets in the vicinity of the massif are also associated with blocked flow (e.g. Marwitz, 1983; Georgelin and Richard, 1996). The transition from flow over to blocked flow may also reduce the amplitude of lee-waves generated by the massif, which in turn may reduce the wave drag by reducing the height of the topography that the unblocked portion of the flow encounters. Stagnant air generated by blocked flow may also absorb downward propagating trapped lee-waves which leads to lee-wave decay (Smith et al., 2002). In addition ridge-parallel variations in the blocked flow can lead to enhanced precipitation on the windward side by enhancing low-level convergence (Rotunno and Ferretti, 2001). A gap exists however between the theory used to predict blocked flow in idealized settings and the application of that theory in the real atmosphere. In particular the thermodynamic structure in the real atmosphere deviates, sometimes substantially, from the theoretical assumptions made in idealized models used to predict blocking.

Two relatively simple theories have been presented to describe the parametric dependence of the blocked flow on the atmospheric structure and the shape of a mountain. Both theories are directly applicable to situations in which the upstream winds are uniform at speed U and the mountain has a simple convex shape with

characteristic along-stream width a, cross-stream width b, and height h_0.

The first theory, proposed by Smith (1988) for circular mountains and extended by Smith (1989) to include elliptical mountains with varying horizontal aspect ratio, $\beta = b/a$, estimates the conditions under which blocking occurs using linear theory of air flow over an isolated mountain in which both the cross-mountain wind speed U and Brunt-Väisälä frequency, N are constant upstream. We label this theory the continuously-stratified constant-stratification (CSCS) theory. Neglecting Coriolis forces and assuming the motions are incompressible, hydrostatic and steady, one may show that the flow is completely determined by two parameters: the mountain height normalized by a scale for the vertical wavelength of a linear gravity that can remain stationary with respect to the mean flow $\epsilon = Nh_0/U$ and β. The parameter ϵ can also be thought of as describing the non-linearity of the flow since the perturbation u in the linear limit is proportional to Nh_0. Smith (1989) found that as ϵ increases, stagnation in the fluid first occurs on the windward slope for narrow mountains ($\beta < 1$) elongated in the direction of the flow and occurs first above the lee-slope in the form of wave breaking for wide mountains ($\beta > 1$). Numerical studies by Smolarkiewicz and Rotunno (1990), Ólafsson and Bougeault (1996), and Bauer et al. (2000) have confirmed the general shape of Smith's curve for stagnation.

The CSCS theory has been extended to account for rotational effects (Thorsteinsson and Sigurdsson, 1996). Using a numerical model they showed that as the influence of rotation increases the value of ϵ required for blocked flow also increases. More recently the effect of air impinging upon a mountain from various flow angles under the influence of rotation has been investigated by Zangl (2004). He found that for a east-west oriented ridge the flow splitting point moves eastward as the ambient flow shifts from northwest to northeast.

Buzzi et al. (1998); Schneidereit and Schär (2000); Rotunno and Ferretti (2001) all examined the effect of latent heat release on flow blocking during the 1994 Piedmont Flood with the aid of numerical simulations. They found that latent heating caused

by condensation reduces the tendency for flow to be blocked by reducing the static-stability upstream on the mountain. In idealized numerical experiments Jiang (2003) showed that latent heat release can can delay the occurrence of flow splitting to values of ϵ twice as large as a dry but otherwise similar atmosphere.

The CSCS theory has been applied by several authors to describe upstream conditions when flow blocking is present. Two methods have appeared in the literature to map atmospheric profiles with non-constant stability to a constant value that can be used to define ϵ. The first is a bulk estimate of the low-level stability where the total change of θ across a layer is used to define N. This method was used by Kitabayashi (1977) in a study of windward stagnation in Japan. Manins (1982) commented that the bulk estimation was inappropriate since at night time it is influenced to much by radiatively cooled surface air. The second method used is to average the low-level stability. This has been used by several authors to estimate the low-level stability (e.g. Manins, 1982; Mass and Ferber, 1990).

The second simple theory that has been used to estimate the threshold for flow blocking relies on the two-layer reduced-gravity shallow-water (RGSW) model. Once again Coriolis forces are neglected; the flow is assumed steady and, consistent with the shallow-water approximation, the motions are assumed to be incompressible and hydrostatic. Let H be the depth of the shallow-water layer upstream and g' the gravitational restoring force on the fluid computed as $\frac{\Delta\rho}{\rho_0}g$ where $\Delta\rho$ is the density difference between the two fluid layers and ρ_0 is the density of the lower layer. According to this model, the disturbance is governed by two key parameters in the upstream flow, the mountain height normalized by the fluid depth $M = h_0/H$ and a Froude number $Fr = U/\sqrt{g'H}$. The RGSW model parameter space has been explored in the laboratory with tank experiments by Lamb and Britter (1984) and with a numerical model by Schär and Smith (1993).

While the RGSW theory has been used by several authors to describe effects in the lee of mountains (e.g. Smith and Grubisic, 1993; Mobbs et al., 2005) it does

not seem to have been widely used to predict upstream stagnation. Chen and Feng (1995) comment that typical values M and Fr during the Hawaiian Rainband Project were in the part of the parameter space in which blocking should be expected. More recently Jiang et al. (2005) used the RGSW theory to characterize blocking during the Mesoscale Alpine Project.

Neither theory, however, exactly accounts for thermodynamic structures like those often encountered in the real atmosphere. In this paper we consider a upstream thermodynamic profile in which an inversion is present near mountain-top level and the remainder of the atmosphere is stably stratified with constant stratification. This profile is a natural extension to both the CSCS theory, because an inversion is introduced into the constant N environment and to the RGSW theory, because background stability and a finite-thickness inversion is introduced into what should otherwise be two homogeneous layers separated by an infinitesimally-thin inversion. In order to keep the parameter space relatively small we consider cases in which the background wind speed is constant with height.

In this study we ask whether the CSCS or RGSW theory gives a better prediction of the likelihood of flow blocking when an upstream inversion is present in a stably-stratified atmosphere. We consider three metrics to characterize the degree of blocked flow: the presence of reversed flow on the windward slope, the minimum wind speed on the windward slope, and the percent of mass initially upstream of the mountain that deviates laterally around the mountain. We test how each idealized method compares with each other in these metrics. In addition to examining whether the RGSW or CSCS theories better predict flow blocking we also examine the best way to map soundings with inversions into the CSCS parameter space. In particular we examine whether the bulk method or the average method is better suited to estimate the low-level stability.

Chapter 2

EXPERIMENTAL SETUP

2.1 Upstream Soundings

The effect of upstream inversions on the upwind side of mountain ranges has seen little attention in the literature. As discussed in the Chapter 1 it is commonplace to smooth an upstream sounding with an inversion so that the stability is constant and the CSCS theory can be applied, or to approximate the inversion with infinitesimally-thin fluid interface so the RGSW theory can be applied. Each method obviously introduces errors into the upstream sounding. This section describes the structure of the upstream sounding with an inversion and how we approximate that sounding to fit into either the CSCS theory or the RGSW theory.

We choose an upstream soundings with an inversion at or below the level of the mountain crest. The solid lines in Fig. 2.1 show the θ profile of two such soundings. The location of the inversion is defined to be where its upper edge is located relative to the top of the mountain. Figure 2.1a shows an inversion where the upper edge is below-mountain-top of a 1000 m high mountain, we call this the "below-mountain-top inversion." The upper edge of the below-mountain-top inversion scales with the mountain height and is located at $z = \frac{3}{4}h_0$, where h_0 is the mountain height. Figure 2.1b shows an inversion where the upper edge is at the mountain-top for the same 1000 m high mountain, we call this the "mountain-top inversion." Like the below-mountain-top inversion the upper edge of the mountain-top inversion scales with the mountain height and is located at $z = h_0$. The thickness of the inversion also scales with the mountain height and is $\frac{1}{4}h_0$. The stability within the inversion as well as

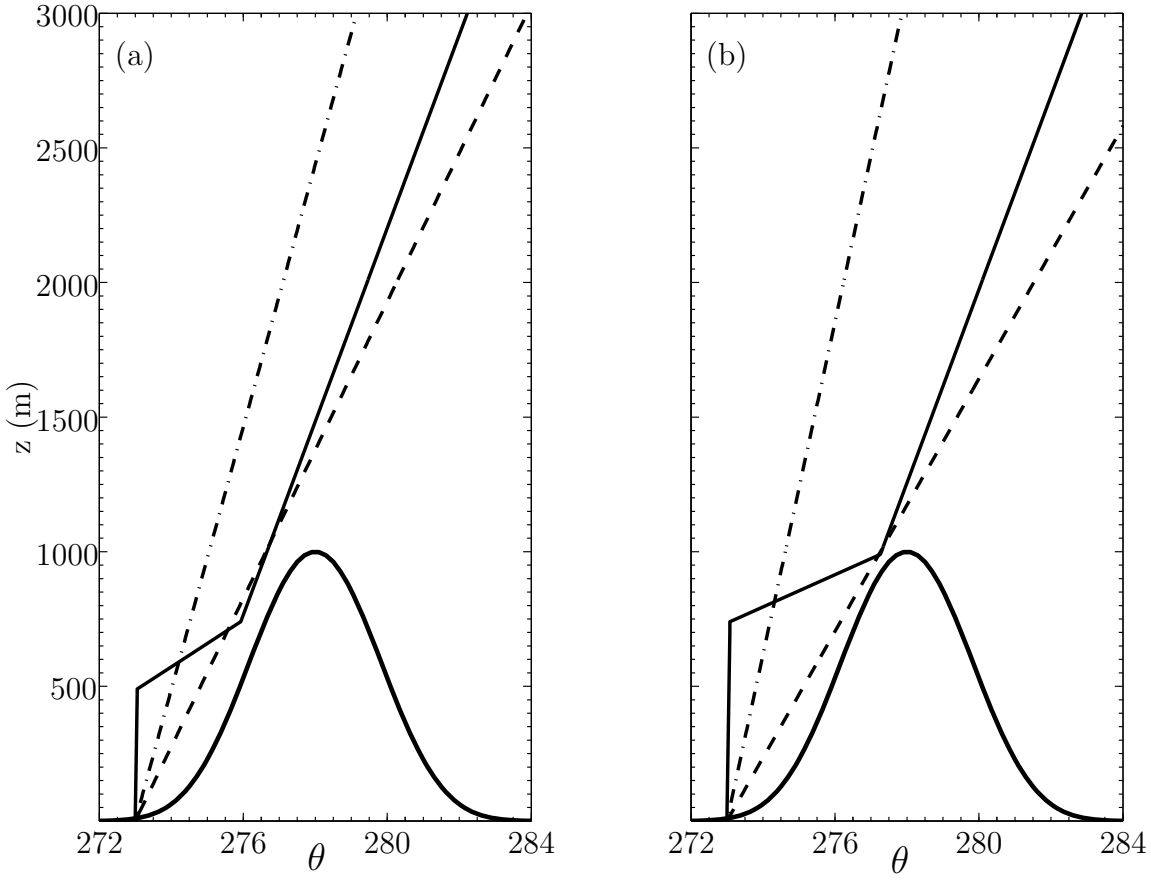

Figure 2.1: Upstream soundings of θ. Solid line indicates the actual sounding for the (a) below-mountain-top inversion and (b) mountain-top inversion for this particular $h_0 = 1000\ m$ high mountain. The dash-dot line is the θ sounding with stability obtained by averaging the stability below-mountain-top line. The dashed line is the θ sounding with stability obtained by making a bulk estimate of the stability below-mountain-top line.

above and below the inversion is constant with height and is independent of h_0. Below the inversion the stability is $N = 0.002\ s^{-1}$ and above the inversion the stability is $N = 0.01\ s^{-1}$. The stability within the inversion varies between the below-mountain-top inversion sounding and the mountain-top inversion sounding and will be discussed later in this section.

If one wishes to apply the CSCS theory to a situation where the upstream sounding has a non-uniform thermodynamic profile then some smoothing operation must be performed on the low-level stability. The stability of the thermodynamic profile must be constant with height in order for the CSCS theory to be directly applicable. We consider two ways to smooth the stability in the upstream soundings with inversions so the CSCS theory is applicable. The first method is to make an average estimate of the stability below the mountain-top,

$$N_A = \frac{1}{h_0} \int_0^{h_0} N(z) dz \tag{2.1}$$

where $N(z)$ is the vertical profile of the Brunt-Väisälä frequency . The θ profile obtained by averaging the low-level stability is shown by the dash-dot line in Fig. 2.1. The second possible method is to make a bulk estimate of the low-level stability by considering the bulk change of θ between the ground and the height of the mountain-top and then define the stability with this,

$$N_B = \sqrt{\frac{g}{\theta_0} \frac{\Delta\theta}{h_0}} \tag{2.2}$$

where $\Delta\theta = \theta(h_0) - \theta(0)$. This is equivalent to averaging N^2 between 0 and h_0. The θ profile obtained by making a bulk estimate of the low-level stability in the inversion sounding is shown by the dashed line in Fig. 2.1. Apparent in Fig. 2.1 is that neither sounding accurately approximates the upper level stability of the sounding with an inversion. The average estimate underestimates the upper level stability while the bulk estimate overestimates it. In order to not introduce any bias in the approximation of the soundings, in particular the stability above the inversion, we set the stability

within the inversion so that the magnitude of the error introduced in N_A and N_B by making the average and bulk approximations, respectively, is equal above the inversion. The stability within the inversion for the below-mountain-top inversion is $N = 0.020\ s^{-1}$ and $N = 0.025\ s^{-1}$ for the mountain-top inversion.

Since there exists no analytic solution to the fully non-linear equations that describe stratified flow over topography with a constant upstream stability profile (CSCS model) we must rely on numerical simulations to evaluate the flow behavior. We map out the ϵ dependence in the CSCS parameter space for three mountain shapes, $\beta = 1$, $\beta = 2$, and $\beta = 4$, by varying the upstream constant stability between N_A and N_B and by varying the mountain height h_0. The numerical model used is described in the next section.

If one wishes to apply the RGSW water theory to a stably stratified sounding with a low level inversion then two variables must be approximated from the upstream sounding. The first is an approximation of the height of the fluid interface far upstream, H_{SW}. Since the inversion has finite thickness, the level of the fluid interface must be arbitrarily chosen to be somewhere within the inversion. We choose the fluid interface to be half-way between the top and bottom of the inversion. We show later though that the the RGSW prediction of flow reversal is sensitive to the choice of the upstream fluid interface height. We also must approximate the reduced gravity, g'_{SW}. We do this by considering $\Delta\theta$, which is now the change of θ across the inversion and θ_0, the potential temperature at the base of the inversion,

$$g'_{SW} = \frac{\Delta\theta}{\theta_0} g. \tag{2.3}$$

With these two parameters we can estimate the upstream Froude number, $Fr_{SW} = U/\sqrt{g'_{SW} H_{SW}}$ and the mountain height normalized by the upstream fluid depth, $M_{SW} = h_0/H_{SW}$.

2.2 Numerical Model

The numerical model follows Durran and Klemp (1983) and Epifanio and Durran (2001). The model is based on the three-dimensional, non-rotating compressible-Boussinesq equations of motion. It is fully non-linear, non-hydrostatic and employs a free-slip lower boundary. The first order closer scheme of Lilly (1962) is used to parameterize sub-grid scale turbulence. At the top boundary a linear radiation condition based on Klemp and Durran (1983) and Bougeault (1983) and modified by Durran (1999) is used. The model uses a terrain following height coordinate

$$\sigma = \frac{z - h}{z_t - h}$$

where z is the physical height, h is the height of the terrain, and z_t is the top of the domain. In order to prevent unphysical maximum and minimum from developing in the θ field near the edges of the inversion a flux limited advection scheme (LeVeque, 1996) is used to advect θ in cases with inversions. A centered fourth order advection scheme is used in all of the cases with constant upstream stability.

The topography used in the model is an elongated ridge with an uniform-height center section and is defined by

$$h(x,y) = \begin{cases} \frac{h_0}{16}\left[1 + \cos\left(\pi r\right)\right]^4, & \text{if } r \leq 1; \\ 0, & \text{otherwise,} \end{cases} \tag{2.4}$$

where

$$r^2 = \begin{cases} \left(\frac{x}{4a}\right)^2 + \left(\frac{|y| - (\beta-1)a}{4a}\right)^2, & \text{if } |y| > (\beta - 1)\, a, \\ \left(\frac{x}{4a}\right)^2, & \text{otherwise.} \end{cases} \tag{2.5}$$

In the above equations h_0 is the maximum mountain height, a is the along-stream length scale, and β is the ratio of along-stream length scale to cross-stream length scale.

The undisturbed upstream wind speed is $U = 10\ m\ s^{-1}$. The flow is in the hydrostatic limit by setting a such that $\frac{Na}{U} = 10$, where N is the stability aloft.

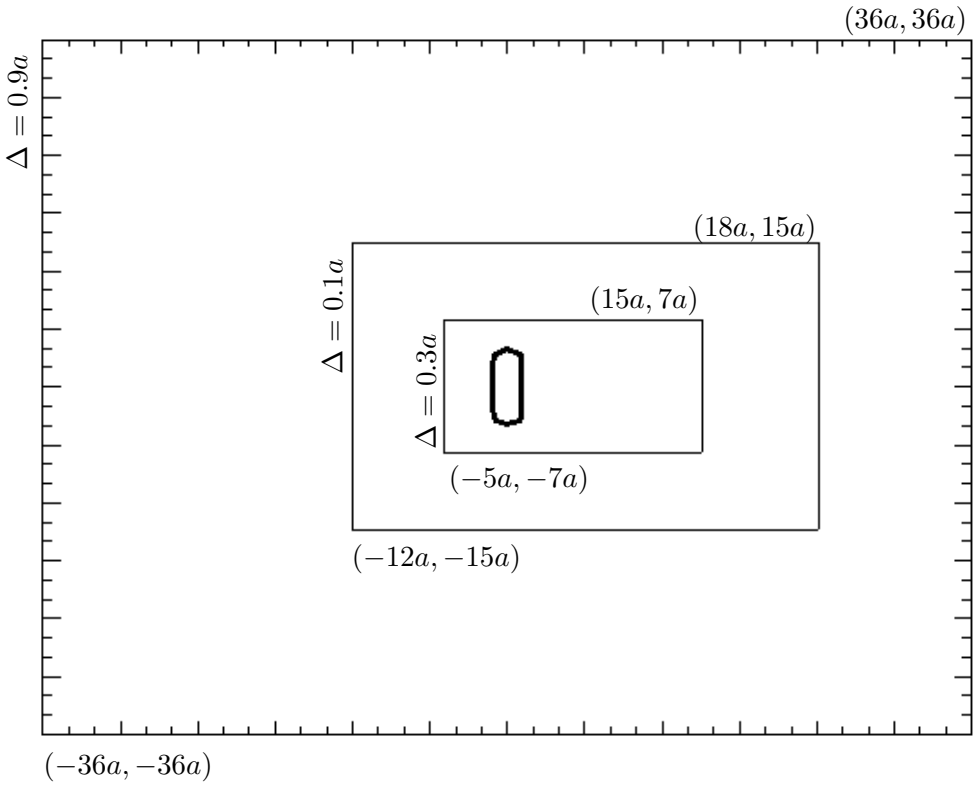

Figure 2.2: Location and size of the three nested grids. Upper right and lower left corner locations are relative to the mountain center.

We initiated the flow by gradually increasing u from rest to U over a time interval $-4 \leq \frac{Ua}{t} \leq 0$. We run the model until $\frac{Ut}{a} = 25$, at which time the upstream flow features are nearly in steady state.

The three nested grids shown in Fig. 2.2 are used in all simulations to make the integration more computationally efficient. The location of the upper-right and lower-left corners of each nest relative to the mountain center, located at the origin, are also shown. The largest nest extends $36a$ in each direction from the mountain center. The second finest mesh extends $-12a$ upstream and $18a$ downstream of the mountain center. The lateral edges of the second finest mesh are $\pm 15a$ from the mountain

center. The finest mesh extends $-5a$ upstream and $15a$ downstream with the lateral edges lying $\pm 7a$ from the mountain center. The horizontal grid spacing is $\Delta = 0.1a$ on the finest mesh and increases by a factor of 3 for each larger mesh. The vertical grid spacing is $\Delta z = h_0/32$ for $z < \frac{3}{2}h_0$ and then stretches to $\Delta z = U/(4N)$, where N is again the stability aloft. This ensures that the inversion will be well resolved with at least 8 grid points while allowing the integration to be computationally efficient. The top boundary is $z_t = \frac{9}{2}\frac{U}{N}\pi$, with N the stability aloft. In order to not violate the CFL condition the large time step on the finest mesh is $\Delta t = 0.025\frac{a}{U}$ and increases by a factor of 3 on each larger mesh.

Chapter 3

FLOW MORPHOLOGY WITH VARYING UPSTREAM SOUNDINGS

3.1 Structure with and without inversions

The morphological flow features present in the solution with an inversion in the upstream sounding are examined in this chapter. In addition morphologic features of solutions with upstream soundings where the stability is constant and estimated from the upstream sounding with an inversion are examined. It should be expected that differences exist between a solution from a a sounding with an upstream inversion and one with constant stability estimated from the inversion sounding, however, since it is very common in the literature to estimate the stability of soundings with non-uniform stability (see Chapter 1) it is important to understand how significant the differences are.

Recall that there are two simple methods we use to estimate an upstream sounding that has non-uniform low-level stability. The first is to average the buoyancy frequency below the mountain crest; the second is to make a bulk estimate of the low-level stability by considering the total change of θ that occurs between the ground and the level of the mountain crest. Neither of these estimates are perfect but recall that the stability within the inversion is set so that the average method underestimates and the bulk method overestimates the upper level stability of the inversion sounding by equal magnitudes. Thus neither the average method or the bulk method is immediately favored when estimated the stability from a sounding with an inversion.

Figure 3.1a shows the u component of velocity and θ contours at a non-dimensional

time of $Ut/a = 25$ for the solution with a below-mountain-top inversion present in the upstream sounding. The mountain height is $h_0 = 1400\ m$ and the mountain aspect ratio is $\beta = 4$ in this figure. Far upstream the top of the inversion is $z = 1050\ m$ and the bottom of the inversion is $z = 700\ m$. The lower edge of the inversion has been displaced upwards by about $300\ m$ at the upstream edge of Fig. 3.1, which is the inflow boundary of the fine-mesh grid.

From the upstream inflow boundary to roughly $x = -1.9a$ the flow field is relatively homogeneous in the vertical direction which is similar to the structure in the RGSW theory where the flow fields are completely uniform below the fluid interface. Downstream of $x = -1.9a$ a horizontal region of reversed flow exists above the mountain surface which extends forward to where it attaches to the mountain surface at about $x = -0.9a$. The magnitude of the u component of the wind is weak within the reversed flow region and does not exceed $2\ m\ s^{-1}$. Fig. 3.2a shows the u component of the wind on the surface in color contours for the same below-mountain-top inversion case. The region of reversed flow runs laterally along the mountain slope to $y = \pm 3.2a$ which is beyond the uniform height section of the ridge. Also shown in blue contours in Fig. 3.2a is the v component of the wind found at the surface. The magnitude of the v component exceeds $2\ m\ s^{-1}$ upstream of $x = -5a$, which is at the edge of the fine-mesh grid. This upstream extent of the cross-stream wind component acts to divert flow laterally around the mountain. The flow diversion will be examined in more detail in Chapter 4.2.

Figures 3.1b and 3.1c correspond to solutions where the upstream soundings are the average estimate and bulk estimate respectively, of the low level stability in the below-mountain-top inversion sounding. The average estimate of the mountain non-linearity parameter in the original sounding is $\epsilon_A = 1.20$ and the bulk estimate is $\epsilon_B = 1.60$. Notice that if the upper level stability is used to define the non-linearity parameter in the sounding with the inversion then $\epsilon = 1.4$ which is $\Delta\epsilon = \pm 0.2$ from either the average or bulk estimates of low-level stability. In both constant-ϵ cases the

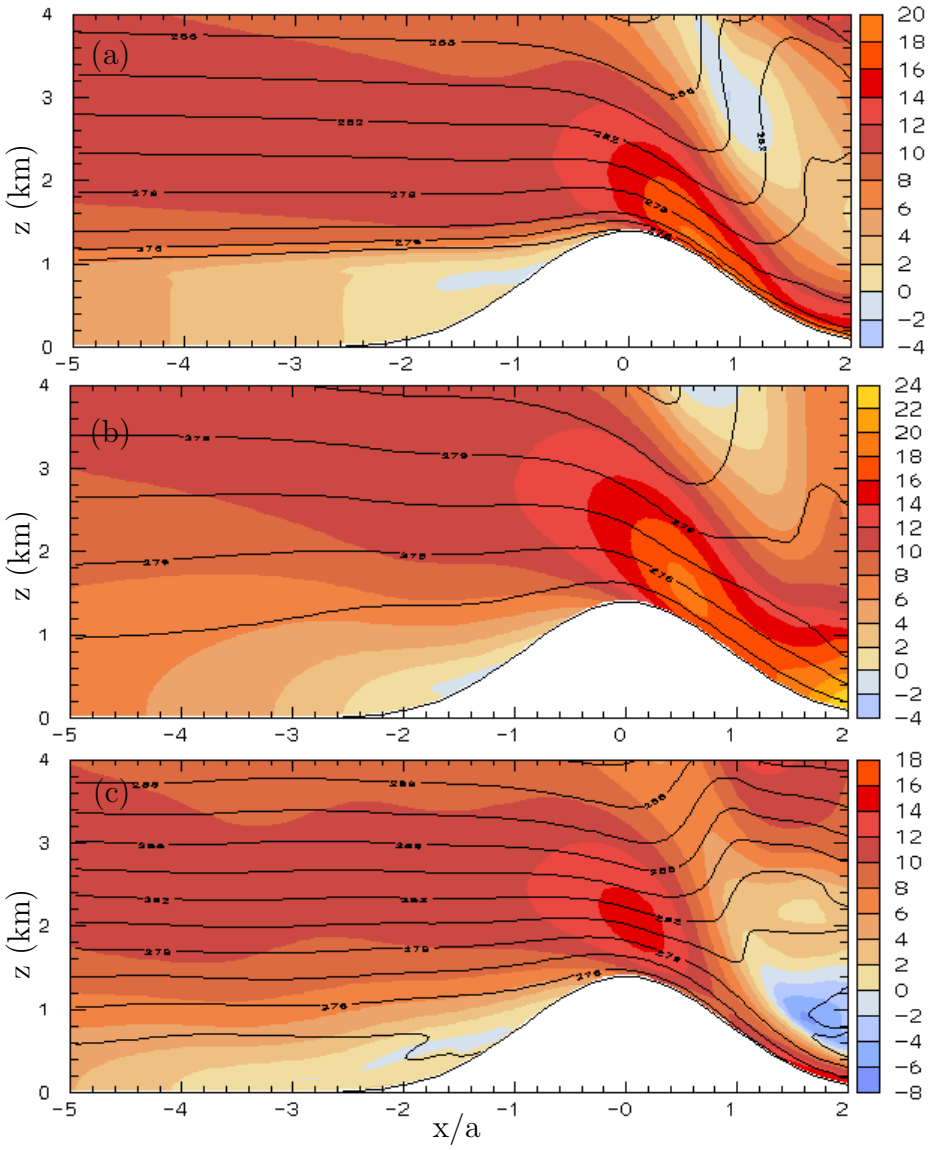

Figure 3.1: The u component of the wind and θ along the center-line of a $\beta = 4$ mountain at $\frac{Ut}{a} = 25$. The solution for the (a) below-mountain-top inversion with physical mountain height of $h_0 = 1400\ m$ and solutions for corresponding constant-N soundings with the stability obtained by: (b) averaging the low-level stability, and (c) making a bulk estimate of the low-level stability.

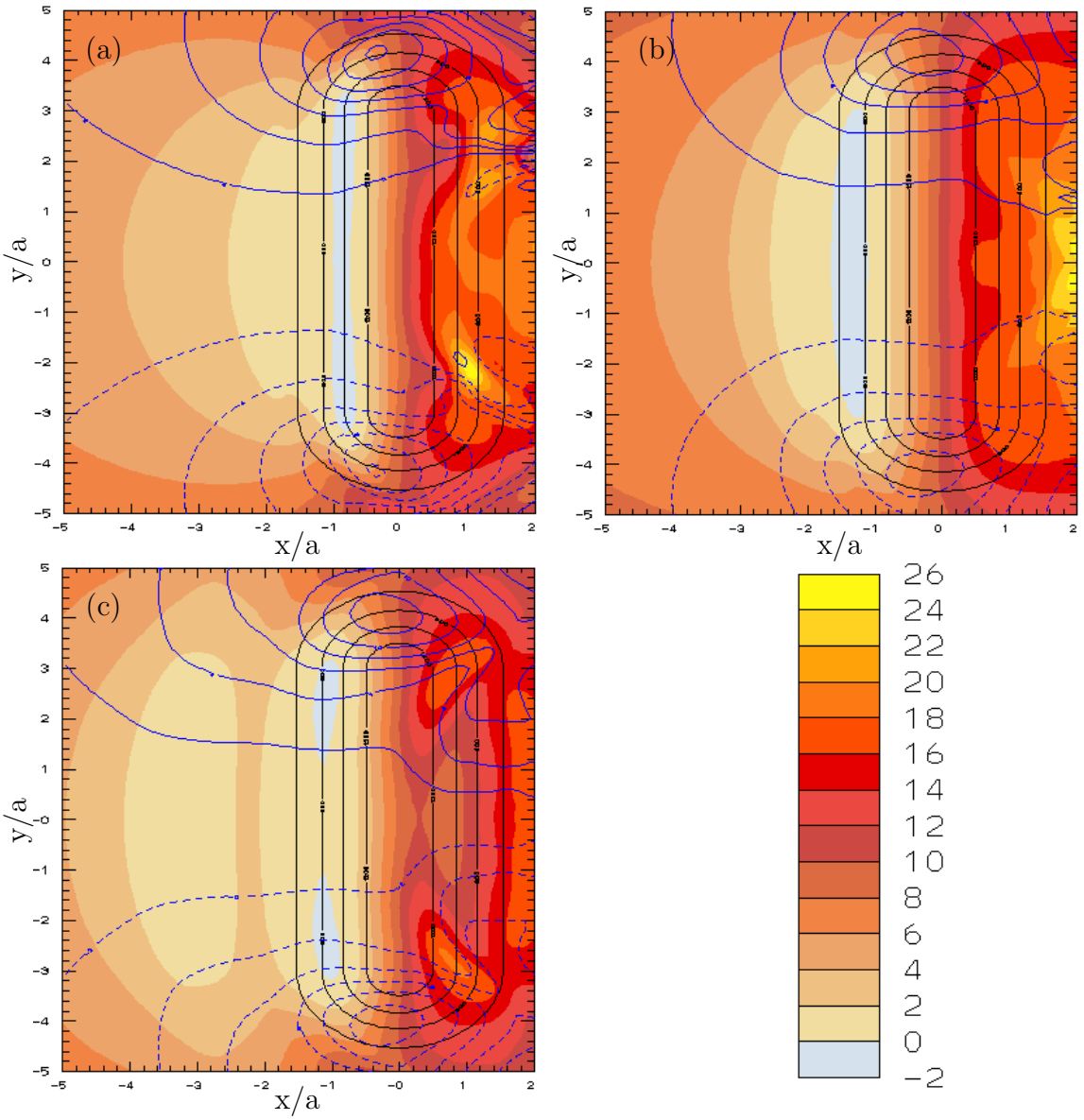

Figure 3.2: The u component of the wind at the surface when $\frac{Ut}{a} = 25$ for a $h_0 = 1400\ m$, $\beta = 4$ mountain is shown in shaded contours, the contour interval is $2\ m\ s^{-1}$. The v component is shown in blue contours with a $2\ m\ s^{-1}$ interval and no zero-line. The case for the (a) below-mountain-top upstream inversion and corresponding constant-N soundings obtained by: (b) averaging, and (c) making a bulk estimate of the upstream stability.

flow is reversed on the upwind side of the mountain. However, in both the average and bulk estimated solutions the flow reversal occurs lower down on the mountain slope than in the below mountain-top inversion case. Also apparent is that in the average estimated sounding the reversed flow remains attached to the surface whereas in the bulk estimated sounding the reversed flow detaches from the surface similar to that in the below-mountain-top inversion sounding. In fact upon closer inspection the reversed flow region in the bulk estimated sounding is not even in contact with the mountain surface. This is also apparent in Fig. 3.2c which shows no reversed flow at the surface along the centerline. Instead reversed flow is present along the outer edges of the uniform height section. This is somewhat of a time dependent feature as the areal coverage of the reversed flow region slowly pulsates on the upwind slope. The reversed flow region at the surface in the solution with the averaged upstream sounding (Fig. 3.2b) extends laterally to roughly the edge of the uniform-height section of the mountain, which is slightly narrower than in the case with a below-mountain-top upstream inversion. Another similarity between the bulk estimated solution and the solution with an inversion is the upstream extent of the v component of velocity. Figure 3.2c shows that the magnitude of the v component exceeds 2 $m\ s^{-1}$ upstream of $x = -5a$, which is at the edge of the fine-mesh grid. In the averaged solution the magnitude of the v component of velocity greater than 2 $m\ s^{-1}$ only extends upstream to roughly $x = -4a$. Consequences of this difference will be explored more in Chapter 4.2 in regards to the low-level flow diversion.

The u component of the wind along with contours of constant θ for the mountain-top inversion case are shown in Fig. 3.3a. This figure is similar to Fig. 3.1a except the upstream inversion is at the mountain-top with the top of the inversion at $z = 1400\ m$ and the bottom of the inversion at $z = 1050\ m$. Like the below-mountain-top inversion, the inversion in this case is displaced roughly 300 m at the upstream edge of the fine-mesh grid. The structure of the flow field is also similar to the below-mountain-top inversion. The u component of velocity is relatively homogeneous in

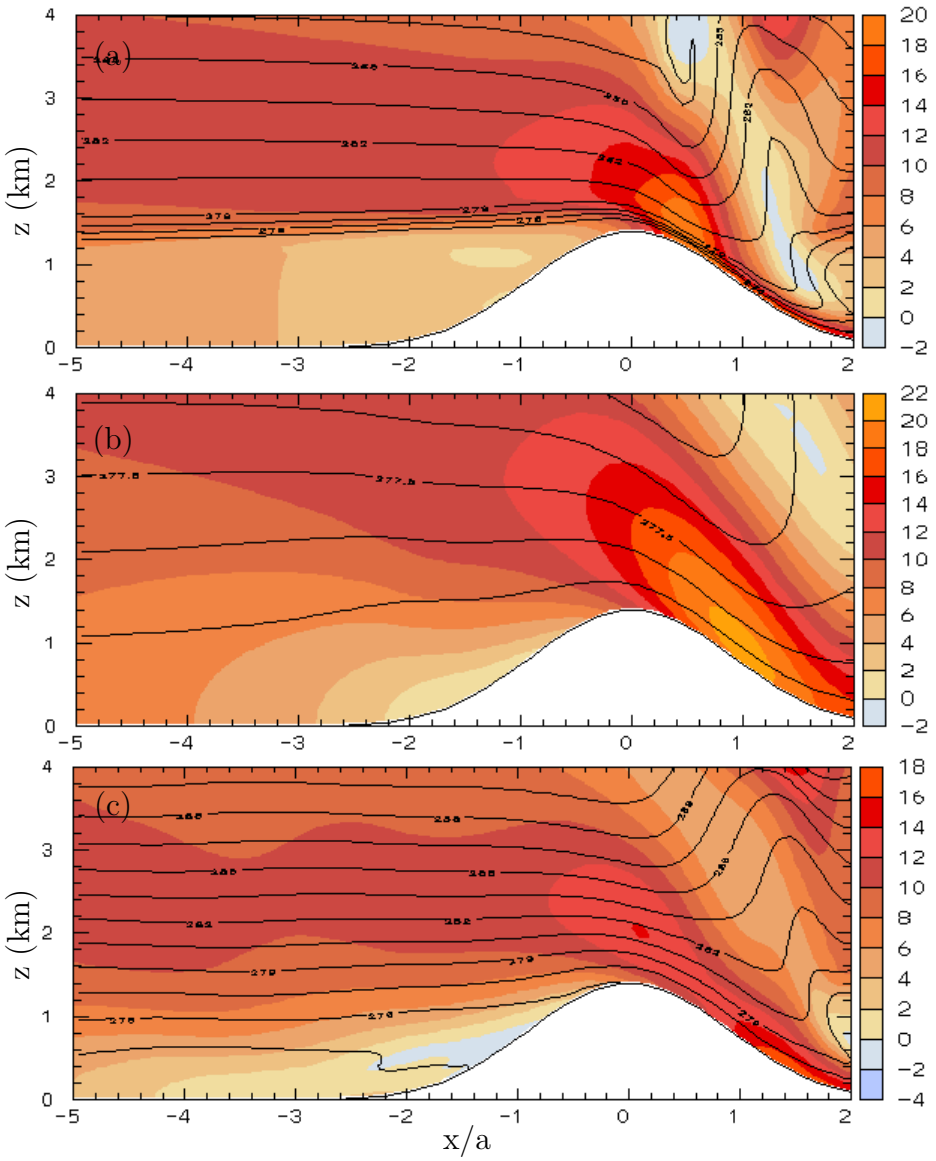

Figure 3.3: The u component of the wind and θ along the center-line of a $\beta = 4$ mountain at $\frac{Ut}{a} = 25$, with $U = 10\ m\ s^{-1}$. The solution for the (a) mountain-top inversion with physical mountain height of $h_0 = 1400\ m$ and solutions for corresponding constant-N soundings with the stability obtained by: (b) averaging the low-level stability, and (c) making a bulk estimate of the low-level stability.

the vertical below the inversion up to roughly $x = -1.8a$. The one main difference between the mountain-top inversion and below-mountain-top inversion solutions is the mountain-top inversion case does not reach a critical mountain height to induce reversed flow on the windward slope. The average estimate of the non-dimensional mountain height obtained from the mountain-top inversion sounding is $\epsilon_A = 1.07$ and the bulk estimate is $\epsilon_B = 1.73$. Here the difference between the average and bulk estimate of the non-linearity parameter and the non-linearity parameter obtained by using the upper level stability in the inversion sounding is $\Delta\epsilon = \pm 0.33$. The solution from the averaged sounding (Fig. 3.3b) also shows that the critical mountain height for reversed flow has not been reached. The flow field instead exhibits a region of non-reversed decelerated flow upstream of the mountain similar to the inversion case. The solution from the bulk estimated sounding (Fig. 3.3c) has reached the critical mountain height and flow reversal is present on the upstream slope. The flow reversal resembles that of Fig. 3.1c where a portion of the reversed flow region is above the surface.

3.2 Sensitivity to stability aloft

In order to determine if the upstream structure is sensitive to the stability aloft several tests were carried out in which the static-stability was varied above height of the inversion. The stability aloft was halved and doubled from the control case, $N = 0.01\ s^{-1}$. These test where conducted for a $\beta = 2$ mountain with a mountain-top inversion at mountain heights surrounding the critical mountain height of stagnation, $h_0 = 1400\ m$ and $h_0 = 1600\ m$.

Figure 3.4 shows the u-component of the wind in shading and θ in contours at $\frac{Ut}{a} = 25$ for the $h_0 = 1600\ m$, $\beta = 2$ mountain. The control run with $N = 0.01\ s^{-1}$ aloft is shown in Fig. 3.4(a). Here, a shallow region of reversed flow exists on the upstream slope between $x = -0.9a$ and $x = -0.6a$. The strength of the the reversed

flow is weak with a minimum wind speed of $u = -0.73\ m\ s^{-1}$. Figure 3.4(b) identical low-level stability structure as in Fig. 3.4(a) but the upper-level static-stability is $N = 0.005\ s^{-1}$. The region of reversed flow for this case is a bit larger extending down the slope to roughly $x = -a$. The magnitude of the reversed flow is also slightly larger with a minimum wind speed of $u = -0.91\ m\ s^{-1}$. Figure 3.4(c) shows the a solution where the static-stability aloft has been doubled from the control solution to a value of $N = 0.02\ s^{-1}$. Here the region of reversed flow is smaller than the control solution, extending down the slope to $x = -0.8a$. The minimum wind speed is $u = -0.51\ m\ s^{-1}$ within the reversed flow. The structure upstream of the reversed flow looks similar in all three cases with the flow being relatively homogeneous in the vertical below the inversion. Similar patterns are seen for the varying stabilities aloft when $h_0 = 1400\ m$ (not shown).

The effect of increasing (decreasing) the stability aloft slightly decreases (increases) the extent of reversed flow on the upstream slope and decreases (increases) the magnitude of reversed flow strength. This result can be understood by considering the effect the stability aloft has on removing perturbations of flow speed variations through gravity wave radiation. The higher stability aloft is more efficient in removing speed perturbations by upward gravity-wave radiation than the lower stability aloft. Thus the reversed flow region and magnitude is smaller with the higher stability aloft.

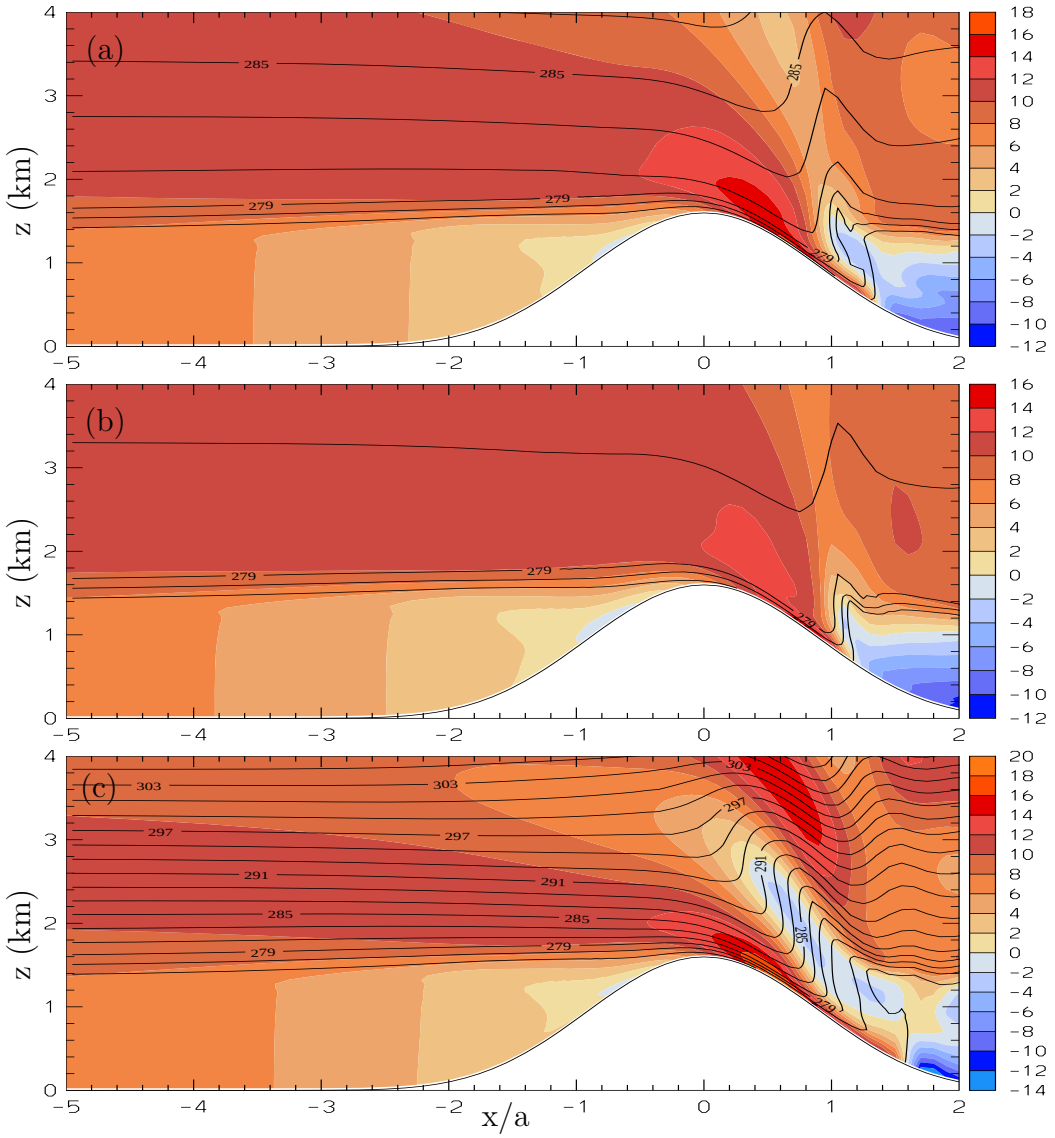

Figure 3.4: The u component of the wind and θ along the center-line of a $\beta = 2$ mountain at $\frac{Ut}{a} = 25$ for various stabilities aloft and $U = 10\ m\ s^{-1}$ far upstream. The solution for (a) $N = 0.01\ s^{-1}$ aloft, (b) $N = 0.005\ s^{-1}$ aloft, and (c) $N = 0.02\ s^{-1}$ aloft.

Chapter 4

PARAMETER SPACE MAPPINGS

As discussed earlier the CSCS model and the RGSW models are described by simple two dimensional parameter spaces. In the CSCS model flow is controlled entirely by ϵ, the mountain height scaled by the vertical wavelength of a linear hydrostatic mountain wave, and β, the ratio of cross-stream to along-stream mountain scales. The RGSW solution is controlled completely by M, the mountain height scaled by the upstream fluid depth, and Fr, the upstream Froude number defined as the ratio of upstream flow speed to the phase speed of a linear gravity wave. Neither of these parameter spaces uniquely determine the solution when an inversion is present in otherwise continuously stratified flow. This Chapter examines if estimating parameters from either the CSCS theory or the RGSW theory using soundings with upstream inversions gives similar results to the solution at the actual point in the respective parameter spaces with regard to various criteria that describe flow blocking.

4.1 Stagnation on the Windward Slope

The first flow-blocking criteria we examine is the presence of stagnation and flow reversal on the windward slope. In the CSCS theory windward side stagnation is synonymous with an isentropic surface being pierced by the mountain surface (Smith, 1988). In the RGSW model if the fluid interface is pierced by the mountain then a stagnation point develops on the windward slope. However it is not completely clear that the mountain-top must pierce the fluid surface for a stagnation point to develop. As shown in Fig. 4.1 one can imagine a situation where two stagnation points develop

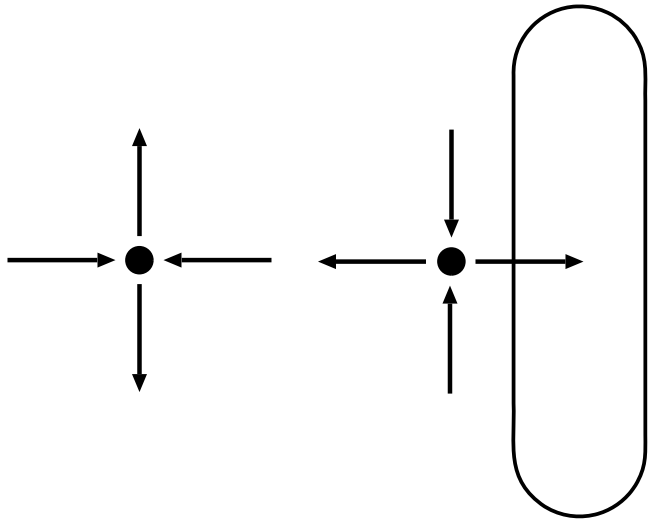

Figure 4.1: Possible flow configuration with non-vanishing fluid depth at the upstream stagnation points. Large represent stagnation points.

upstream of the mountain with a region of reversed flow between them. It would not be necessary for the fluid depth to vanish at either stagnation point in Fig. 4.1. In this thesis however, we assume that stagnation does indeed occur simultaneously with the mountain piercing the fluid surface as numerical simulations by Schär and Smith (1993) suggest to be the case. However future work should be directed toward showing that the fluid depth must vanish when the upstream flow stagnates with either numerical simulations or an analytic proof.

To determine the critical value $\widehat{\epsilon}$, at which stagnation occurs for three mountain shapes, $\beta = 1$, $\beta = 2$, and $\beta = 4$ in the CSCS theory, the numerical model described in Chapter 2.2 was run with the constant stability upstream soundings obtained from the average estimate or bulk estimate of the soundings with inversions to a

non-dimensional time of $Ut/a = 25$. The flow structure at this time is relatively steady on the windward slope. The parameter ϵ was varied by both increasing the mountain height in 200 m increments and varying the upstream stability between values obtained by averaging or making a bulk estimate of the stability in the sounding with an inversion. The critical non-linearity parameter, $\widehat{\epsilon}$ was determined by linearly interpolating between the two values of ϵ in which stagnation occurs in one simulation and not in the other.

To determine the critical parameters, $\widehat{M}$ and $\widehat{Fr}$, at which stagnation occurs in the RGSW theory an analytical prediction derived by both Lamb and Britter (1984) and Schär and Smith (1993) and re-derived here is used. The prediction assumes that the mountain-top dries out with the development of a windward stagnation point. As discussed above this assumption may not be necessary for stagnation but numerical simulations by Schär and Smith (1993) suggest it to be the case. The derivation makes use of conservation of Bernoulli's function for shallow water flow

$$B = \frac{1}{2}\mathbf{u}\cdot\mathbf{u} + \mathbf{g}(\mathbf{H}+\mathbf{h}) \tag{4.1}$$

to relate the undisturbed conditions far upstream and the conditions at the stagnation point. If the upstream flow is unidirectional with speed U and depth H and the fluid depth vanishes at the stagnation point where the hill height is h_s, then since the flow is steady and inviscid we can equate the Bernoulli function along a streamline that stretches from far upstream to the stagnation point,

$$gh_s = \frac{1}{2}U^2 + gH.$$

Therefore stagnation will only occur when $h_0 \geq h_s$, with the critical hill height found at the equality. Thus stagnation occurs whenever

$$gh_0 \geq \frac{1}{2}U^2 + gH. \tag{4.2}$$

Dividing the above equation by gH and using the definition of M and Fr leads to

the stagnation condition of

$$M \geq \frac{1}{2}Fr^2 + 1 \tag{4.3}$$

with $\widehat{M}$ and $\widehat{Fr}$, the critical non-dimensional height and Froude number found at the equality. Using the equality on (4.3) and rearranging shows that

$$\widehat{Fr} = \sqrt{2(\widehat{M} - 1)}. \tag{4.4}$$

If $\widehat{M} \leq 1$ the upstream fluid interface is at or above the height of the hill and stagnation is not possible in the RGSW theory.

Schär and Smith (1993) showed that that even though the fluid depth vanishes at the stagnation point the Froude number remains well behaved in a region around the stagnation point and also vanishes at the stagnation point. Thus if the flow is sub-critical upstream it remains sub-critical near the stagnation point.

Plotted in Fig. 4.2 is the difference between the critical values, $\widehat{\epsilon}$ or $\widehat{Fr}$, from the respective CSCS model (obtained by numerical simulations) and RGSW theory, obtained by (4.4), and the critical values of ϵ and Fr estimated from the upstream sounding with inversions, obtained by numerical simulation. Figure 4.2a shows the difference for the below-mountain-top inversion and Fig. 4.2b is for the mountain-top inversion. As discussed in Chapter 2.1 there are two ways to estimate the value of ϵ from a sounding with an upstream inversion. The first estimate considers the bulk change of θ below the mountain-top to determine ϵ while the second method considers the average buoyancy frequency below mountain top. The bulk and average estimates of ϵ are labeled ϵ_B and ϵ_A respectively. The upward pointing triangles in Fig. 4.2 represent the difference between the critical value, $\widehat{\epsilon}$ in the CSCS model found by numerical simulations, and the critical value $\widehat{\epsilon}_B$, the bulk estimate of the non-linearity parameter, at which stagnation occurs in the simulation with an upstream inversion, relative to $\widehat{\epsilon}$,

$$\Delta S_B = \frac{\widehat{\epsilon}_B - \widehat{\epsilon}}{\widehat{\epsilon}}.$$

The downward pointing triangles represent the relative difference between $\widehat{\epsilon}$ from numerical simulations of the CSCS model and $\widehat{\epsilon}_A$, the average estimate of the non-linearity parameter at which stagnation occurs in the simulation with an upstream inversion,

$$\Delta S_A = \frac{\widehat{\epsilon}_A - \widehat{\epsilon}}{\widehat{\epsilon}}.$$

In both the the below-mountain-top inversion case (Fig. 4.2a) and the mountain-top inversion case (Fig. 4.2b) the value at which the flow stagnates in the CSCS theory is better estimated by averaging the low level stability as opposed to using the bulk estimate. The bulk estimate of low level stability consistently over estimates the value of $\widehat{\epsilon}$. It is interesting that the error introduced by both the average and bulk estimate in determining the $\widehat{\epsilon}$ in the CSCS model is relatively independent of β. This is especially true for the below-mountain-top inversion case (Fig. 4.2a). This suggests that the dependence of the stagnation point on β in the CSCS theory is unaffected by the presence of an inversion.

The circles in Fig. 4.2 represent the difference between $\widehat{Fr}$ and Fr_{SW} relative to $\widehat{Fr}$,

$$\Delta S_{SW} = \frac{\widehat{Fr}_{SW} - \widehat{Fr}}{\widehat{Fr}}.$$

$\widehat{Fr}_{SW}$ is the estimation of the Froude Number at the critical mountain height of stagnation found in the solution with an upstream inversion. The parameter $\widehat{Fr}$ is the critical mountain height predicted by (4.4) with $\widehat{M}_{SW}$ estimating the non-dimensional mountain height. Since M in the RGSW represents the height of the mountain relative to an infinitesimally thin interface some ambiguity is present when approximating the fluid interface with an inversion of finite thickness. Therefore error bars are plotted along with the circles in Fig. 4.2 to represent the range of ΔS_{SW} when the fluid interface ranges between the top and bottom of the inversion. The circles estimate the interface to be halfway through the inversion. As the estimated height of the interface increases (decreases) in the inversion ΔS_{SW} increases (decreases).

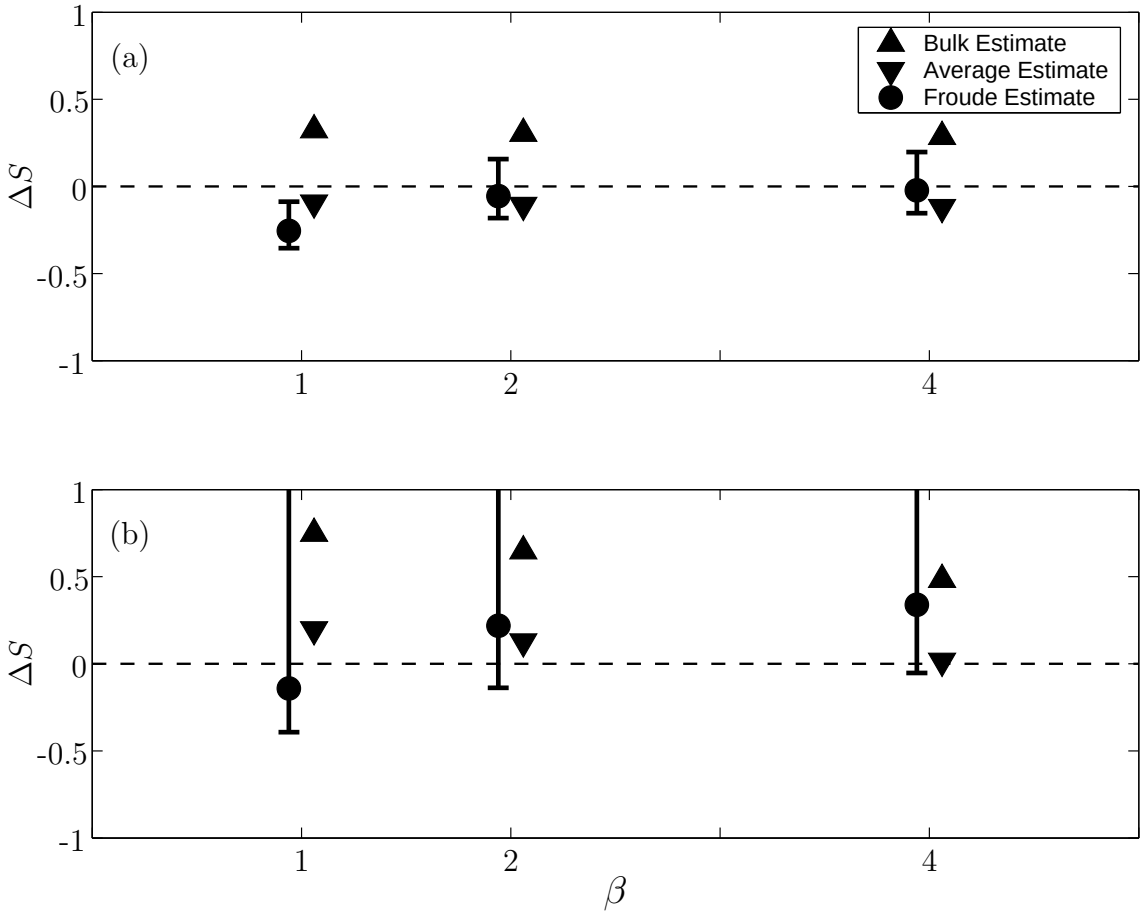

Figure 4.2: The relative difference of the critical value of ϵ and Fr in the respective CSCS and RGSW theories and the critical value of stagnation when ϵ and Fr are estimated from a sounding with an upstream inversion: (a) below-mountain-top inversion, or (b) at mountain-top. Error bars for the RGSW estimate represent the error in choosing a infinitesimally thin fluid interface in an inversion of finite thickness. Data is staggered from $\beta = 1$, $\beta = 2$, and $\beta = 4$ for readability.

Examination of (4.4) revels that if $\widehat{M} \leq 1$ then the RGSW predicts that stagnation will not develop on the windward slope. For the mountain-top inversion case (Fig. 4.2b), as the estimated fluid interface approaches the top of the inversion $\widehat{M}_{SW} \rightarrow 1$, $\widehat{Fr} \rightarrow 0$ and since $\widehat{Fr}_{SW} \neq 0$ $\Delta S_{SW} \rightarrow \infty$, which means that stagnation is occurring in the stratified case with an inversion but it can never happen in the RGSW theory.

Estimating the upstream sounding with parameters from the RGSW model to predict stagnation gives mixed results. For the below-mountain-top inversion (Fig. 4.2a) the method does quite well for $\beta \geq 2$ if the fluid interface is estimated to be in the middle of the inversion (filled circles); however there is some sensitivity to the exact placement of the fluid interface within the inversion which can either increase or decrease the magnitude of ΔS_{SW}. For $\beta = 1$, the averaging estimate for CSCS gives better results.

In the mountain-top inversion case (Fig. 4.2b) when the fluid interface is estimated to be halfway through the inversion ΔS_{SW} increases with β and is quite large relative to the averaging method, ΔS_A. The is also a large sensitivity of ΔS_{SW} to the to the estimation of the fluid interface. This sensitivity to the precise location of the fluid interface would make applying the RGSW model in the real world to predict flow stagnation difficult when the upstream height of the inversion is near the mountain-top.

4.2 Low-Level Flow Diversion

The second flow blocking criteria we examine is the amount of mass initially upstream that is diverted around its lateral sides as opposed to rising freely over the top of the mountain. Comparisons are made between the amount of flow diverted around the mountain in the CSCS theory where the stability is constant and where the low-level stability and non-dimensional mountain height are estimated from an upstream sounding with a low-level inversion present at or below-mountain-top. Comparisons

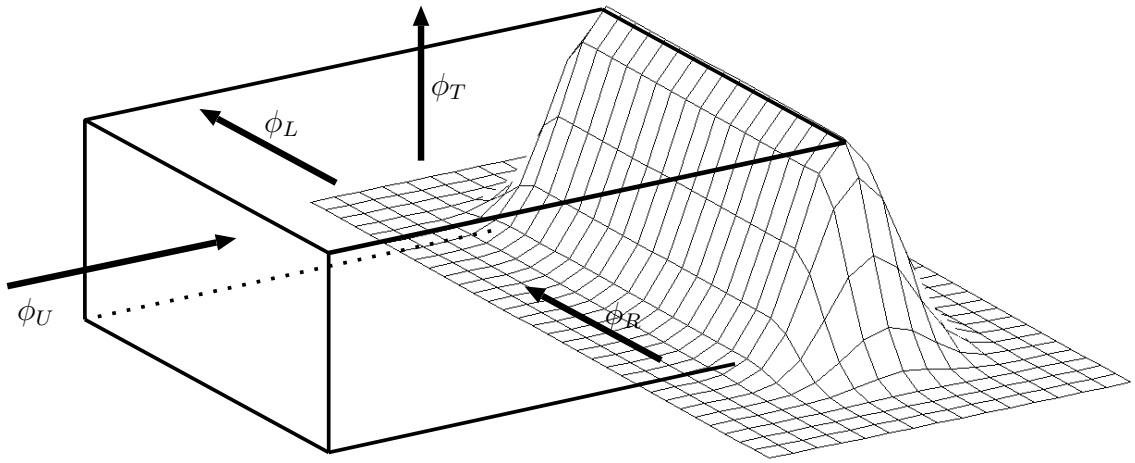

Figure 4.3: Schematic of the control volume for the low-level flow diversion calculation.

are also made between the flow diversion predicted when a stagnation point is present in the RGSW model and the situation with an inversion present in the upstream sounding.

In order to calculate the low-level flow diversion we construct a control volume upstream of the mountain as shown in Fig. 4.3. The flow diversion is calculated on the second grid in order to allow the control volumes upstream boundary to extend maximally upstream. The control volume extends upstream to $x = -12a$ which is at the inflow boundary of the computational grid and downstream to the ridge crest at $x = 0$. The lateral edges of the control volume extends to the edge of the uniform height section of the ridge crest, $y = \pm(\beta - 1)a$. The top of the control volume is a rigid lid at located at the height of the mountain-top, $z = h_0$. Mass must be conserved within the control volume so

$$\int\int \rho_s \mathbf{u} \cdot \mathbf{n} \, \mathbf{dA} = \mathbf{0}, \tag{4.5}$$

where ρ_s is a reference Boussinesq density and the integration is over the surface of the control volume. If ϕ_U, ϕ_R, ϕ_L, and ϕ_T are the integrated mass fluxes over each

surface shown in Fig. 4.3 then (4.5) can be rewritten as

$$\phi_U = (\phi_L - \phi_R) + \phi_T. \tag{4.6}$$

The contribution of mass into the control volume is dominated by ϕ_U thus this can be considered the sole source of mass into the volume. All the mass entering the control volume from the upstream boundary can either ascend through the top of the volume, ϕ_T, or divert laterally around the mountain, $(\phi_l - \phi_r)$. The flow diversion is then defined as the ratio of the mass that diverts laterally around the sides of the mountain to the mass that enters the control volume upstream,

$$FD = \frac{\phi_l - \phi_r}{\phi_u}. \tag{4.7}$$

The calculation for flow diversion was done for the $\beta = 2$ and $\beta = 4$ mountains. The calculation was not done for the $\beta = 1$ mountain since the control volume has zero width in this case.

The low-level flow diversion in the CSCS theory, as computed by the numerical model, for both the $\beta = 2$ and $\beta = 4$ mountains, is shown by the dashed line in Figs. 4.4a and 4.4b respectively. For both mountain shapes the amount of flow diverted around the mountain steadily increases with increasing ϵ. The amount of diverted flow is similar for both $\beta = 2$ and $\beta = 4$ mountains especially for $\epsilon \leq 1.2$. For $\epsilon > 1.2$ the flow diversion increases less rapidly for the $\beta = 4$ mountain than it does for the $\beta = 2$ mountain.

Recall that when estimating the low-level stability two methods are possible: averaging the stability below-mountain-top and using the total change of θ below-mountain-top to define a bulk stability. Therefore each sounding with an upstream inversion has two estimates of ϵ, one for the averaging method and one for the bulk method. The flow diversion for the upstream sounding with a below-mountain-top inversion is shown in Fig. 4.4. The downward pointing triangles represent ϵ_A obtained by averaging the low-level stability and the upward pointing triangles represent ϵ_B

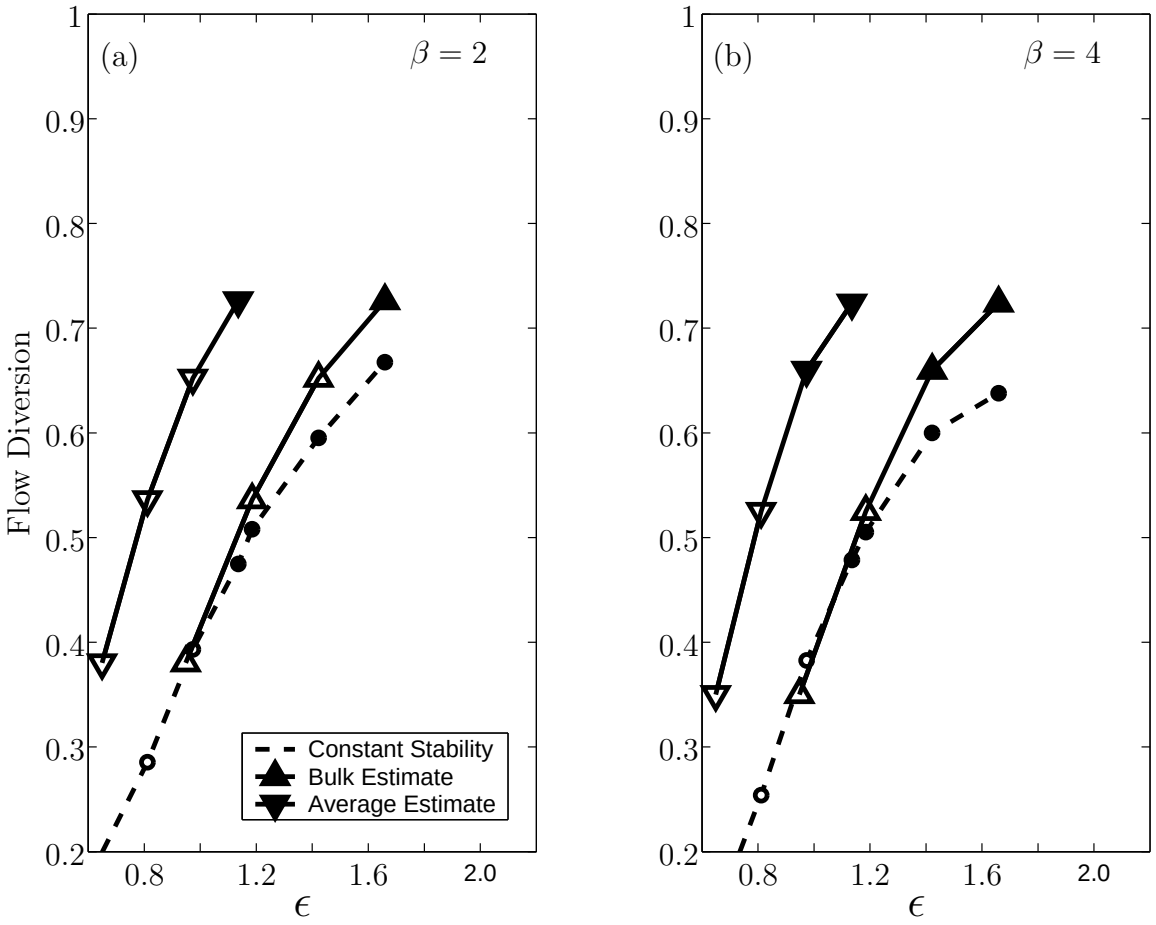

Figure 4.4: Flow diversion around the mountain at $\frac{Ut}{a} = 25$ for mountain shapes (a) $\beta = 2$, (b) $\beta = 4$. The dashed line is the flow diversion for the CSCS theory. The flow diversion for a sounding with an upstream low-level inversion is represented by the two solid lines. The downward and upward triangles represent the low-level stability begin estimated by averaging and the bulk method respectively. Filled triangles and shapes represent the flow is reversed on the windward slope.

obtained by making a bulk estimate. It should be emphasized even though the solid curves in Fig. 4.4 represent two separate ways to estimate the upstream stability and therefore ϵ, the actual upstream sounding and therefore the flow-diversion around the mountain are the same for each pair of triangles.

Examination of Fig. 4.4 reveals that when an upstream inversion is present estimating the low level stability with the bulk method represents ϵ in the CSCS theory for a given flow diversion more accurately than the average method does. For example for the $\beta = 2$ mountain (Fig. 4.4a) $FD = 0.536$ at $\epsilon = 1.25$ computed by the numerical model in the CSCS theory. The bulk method estimates that $\epsilon_B = 1.19$ and the average method estimates that $\epsilon_A = 0.81$ for the flow diversion to be the same as computed in the CSCS model. In all cases the the bulk estimate of the low-level stability does a better job than the average method in reproducing the flow diversion of the constant-stratification situation. The average estimate underestimates the stability and thus underestimates the value of ϵ required to give the correct value of ϵ for a given flow diversion. The accuracy of the bulk mapping is particularly evident for lower values of ϵ and ϵ_B where the two curves almost overlay each other. As the bulk estimate of ϵ increases the flow diversion increases to values greater than that found at equal values of ϵ in the CSCS theory.

As in Fig. 4.4, Fig. 4.5 shows the flow diversion for the constant stratification simulation with dashed lines. Since the dashed curves in Figs. 4.4 and 4.5 represent the same values of ϵ and thus that same points in the CSCS parameter space in principle, they should be exactly the same between corresponding panels of the two figures. The values are, however, taken from two different sets of constant N. Some small discrepancies exist between these pairs of constant N simulations. This is probably due to the flow not begin entirely in a steady state at the time the mass flux calculation was made and non-hydrostatic effects present in the flow which would both violate the scaling arguments presented in Smith and Grønås (1993). Nevertheless the agreement between the dashed curves in both figures far out-weighs the small

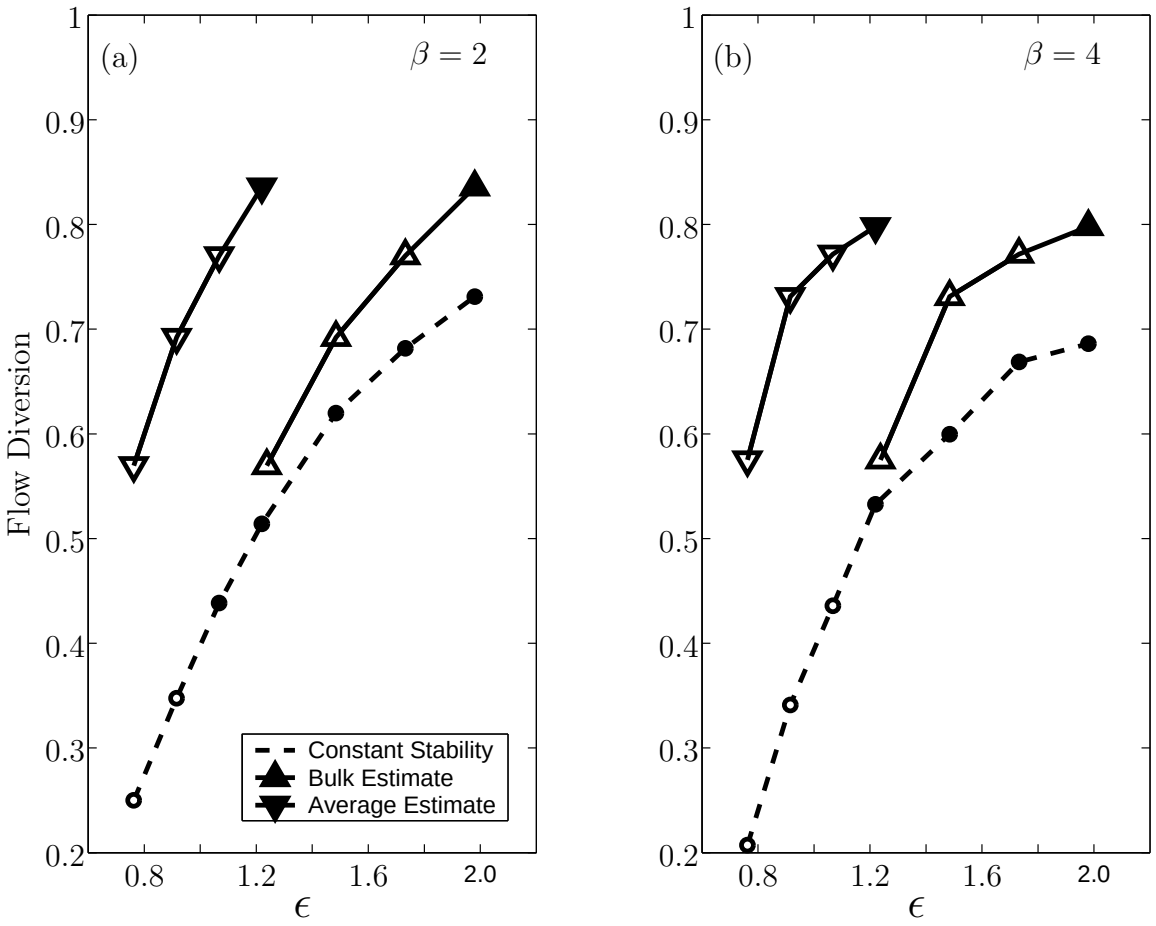

Figure 4.5: Similar to Fig. 4.4 except for the mountain top inversion.

disagreements and is of little importance to the results of this section.

The solid lines in Fig. 4.5 represent curves for the flow diversion from the upstream sounding with an inversion. Again the downward pointing triangles represent ϵ_A, obtained by averaging the low-level stability in the upstream sounding, and the upward pointing triangles represent ϵ_B, obtained by making a bulk estimate of upstream low-level stability. We again see in Fig. 4.5 that the bulk method of estimating the upstream sounding does a better job in representing the true value of ϵ than the average method does. However, the agreement between the bulk estimate and the calculated flow diversion in the CSCS model is not as good as in the below-mountain-top inversion case, especially for the $\beta = 4$ mountain (Fig. 4.5b). As in the below-mountain-top inversion case when $\epsilon > 1.2$ the differences become significant between the diverted flow in the bulk estimated case and the constant stability case. The flow diversion begins to level off in the case with no upstream inversion whereas it continues to increase in the case with an upstream inversion. The increase in flow diversion in the case with a upstream inversion is similar to what would be expected to happen in the RGSW theory where the 100% of the flow must be diverted around the mountain when a stagnation point develops. This is because the top of the mountain dries out when the flow reaches stagnation in the RGSW and thus no flow can pass over the mountain-top. The amount of flow-diversion is around 80% when the flow reverses in the mountain-top inversion case for both the $\beta = 2$ and $\beta = 4$ mountains.

4.3 Minimum Speed on the Windward Slope

The third and final criteria we use to test the degree of flow blocking is how much the upstream flow decelerates as it approaches the ridge crest. This measure of blocking is of course related to the onset of flow stagnation discussed in section 4.1 but gives an evolution of the amount of blocked flow as the parameters change. We again will compare the flow deceleration computed when the upstream stability is constant

and the deceleration experienced when an upstream inversion is present at or below mountain-top. Since we have not run a shallow-water model we do not know the minimum speed on the windward slope in the RGSW theory for mountains to low to force stagnation. Therefore this section will deal exclusively with simulated differences in flow deceleration for a given ϵ in the CSCS theory and the two estimates of ϵ made from the sounding with an upstream inversion.

The minimum u component of wind upstream of the ridge crest from an upstream sounding with constant stability is shown by the dashed lines in Fig. 4.6. All three mountain shapes show that the minimum wind speed gradually decreases as ϵ increases until ϵ is large enough to induce flow reversal. The rate of decrease of the minimum wind speed as a function of ϵ for the elongated mountains (Figs. 4.6b and 4.6c) is much greater than that of the round mountain (Fig. 4.6a). After flow reversal the trend in the minimum wind speed flattens out and even reverses a bit (the minimum wind speed slightly increases with increasing ϵ).

The solid lines in Fig. 4.6 show the minimum wind speed found on the upstream slope when the upstream sounding has a below-mountain-top inversion. Both solid lines represent solutions to an initialization with the same upstream sounding however the way in which the low-level stability was estimated differs between the two. The downward pointing triangles represent the minimum wind speed at values of ϵ_A obtained by making an average estimate of the low-level stability, while the upward pointing triangles represent the minimum wind speed at values of ϵ_B, obtained by making a bulk estimate of the low-level stability. The minimum wind speed curve at values of ϵ_B is shifted to the right of the minimum wind speed curve calculated when the stability is constant with height while the curve with values of ϵ_A is slightly shifted to the left. This indicates that the bulk method overestimates ϵ while the average method slightly underestimates it. The underestimation of the average method seems to be much smaller than the overestimation of the bulk method.

The average method does seem to perform better than the bulk method in esti-

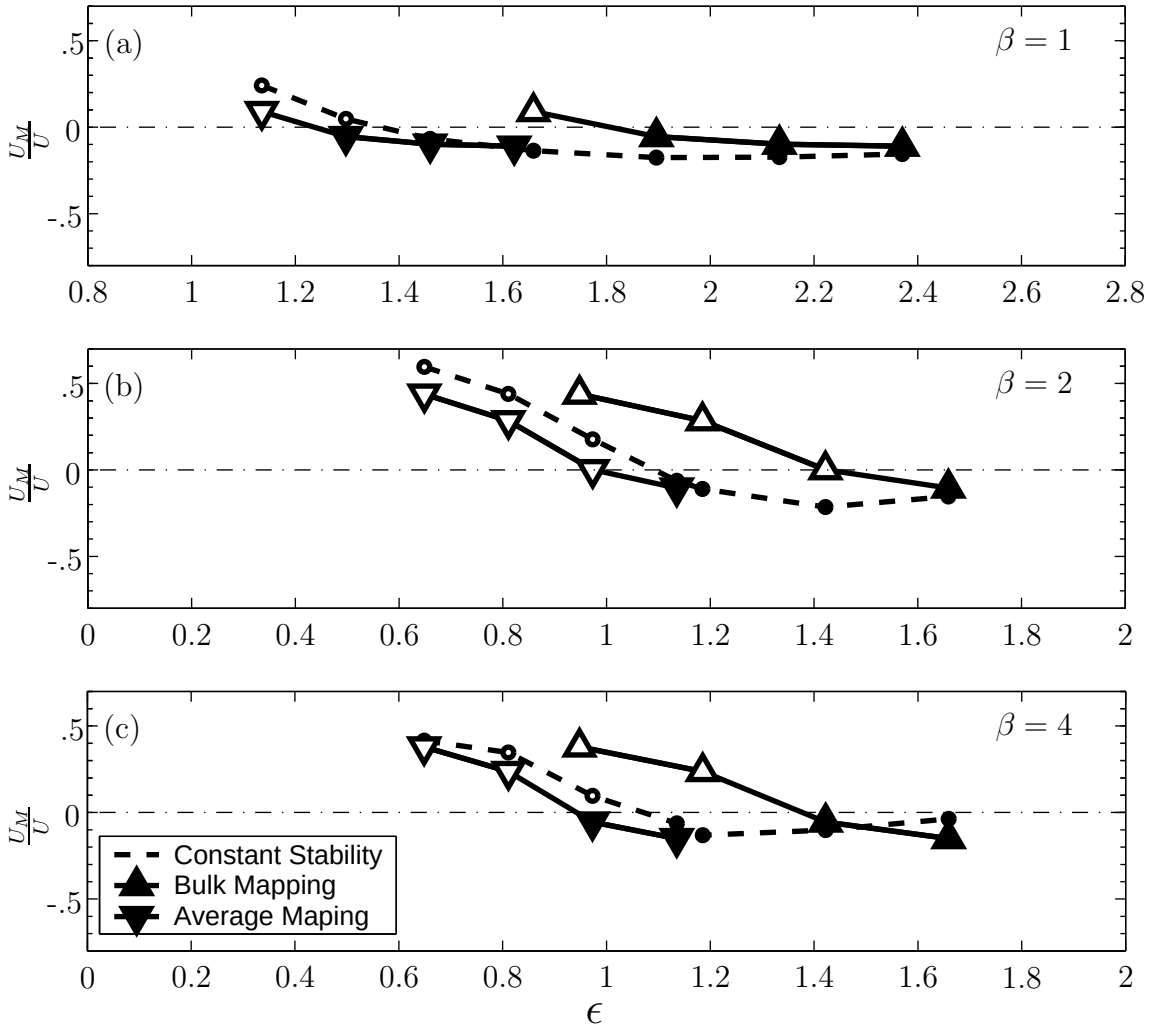

Figure 4.6: Minimum u component of wind on the upstream side of the ridge as a function of ϵ at $\frac{Ut}{a} = 25$ for the constant stability upstream sounding (dashed), upstream below-mountain-top inversion with averaging estimate (downward triangles), and upstream below mountain top inversion with bulk estimate (upward triangles) for (a) $\beta = 1$, (b) $\beta = 2$, (c) $\beta = 4$. Filled triangles and circles indicate the flow has reversed on the windward slope.

mating the correct value of ϵ from the calculated minimum wind speed in the CSCS model. The average method especially does a good job for $\epsilon > 1.4$ with a $\beta = 1$ mountain (Fig. 4.6a). This is in direct contrast to the low-level flow diversion where it was found that the bulk estimate did a better job than the average method in reproducing the correct value of ϵ.

Figure 4.7 again shows the minimum wind speed when the upstream sounding is constant with dashed lines. The solid lines in Fig. 4.7 represent the case when there is a mountain-top inversion present in the upstream sounding. The one striking thing about this figure is that for all values of β the average method does an exceptional job of mapping the actual sounding into the parameter space of the CSCS model. This is particularly evident for the $\beta = 4$ mountain (Fig. 4.7c) where the solid curve representing the average estimate directly overlays the minimum wind speed curve from the CSCS theory. We also see that for the $\beta = 1$ mountain even though the difference between the critical ϵ in the CSCS theory and the critical ϵ obtained by averaging the low-level stability is somewhat large (Fig. 4.2b) the average method of estimating ϵ does a decent job at replicating the minimum wind speed found in the CSCS theory. It is clear from Figs. 4.6 and 4.7 that the averaging method out performs the bulk method when estimating ϵ from a sounding with an upstream inversion in determining the minimum wind speed on the upstream slope.

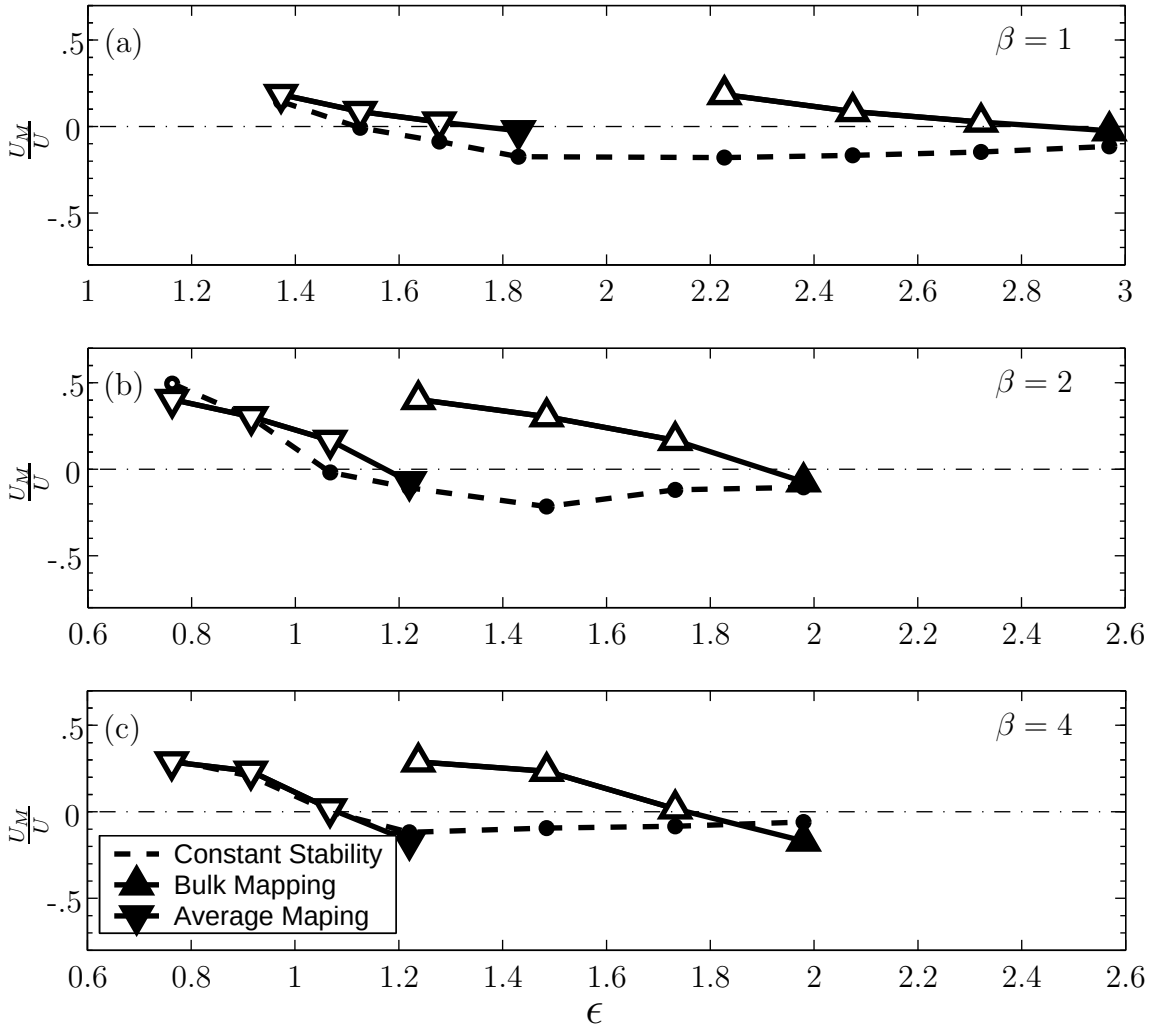

Figure 4.7: Similar to figure 4.6 except for the mountain-top-inversion.

Chapter 5

CONCLUSIONS

Both the CSCS model and RGSW model have simple parameter spaces to describe flow over topography. The CSCS model is described by the parameter ϵ, the mountain height scaled by the vertical wavelength of a linear, hydrostatic mountain wave, and β, the ratio of cross-stream to along-stream mountain scales. The RGSW model is described by M, the mountain height scaled by the upstream level of the fluid interface, and Fr, the upstream Froude Number. While both models describe the parametric dependence of blocking upstream of a mountain in idealized settings, many authors attempt to characterize blocking in the real-world using one of these theories when the upstream sounding deviates from the idealized assumptions. We have therefore conducted a series of numerical simulations with inversions present at or below the mountain-top in the upstream sounding of an otherwise continuously-stratified fluid and compared these solutions to those in either the CSCS model or the RGSW model.

To apply the CSCS model for a sounding with an upstream inversion we examined two possible ways to estimate the parameter ϵ. The first was an average estimate of the stability below mountain-top and the second was a bulk estimate, where the total change of θ below-mountain-top was used to estimate the stability. We found that when windward flow reversal was present in the solution with an inversion, the structure of the reversed flow more resembled the structure of reversed flow in a solution with constant stability upstream obtained from the bulk estimate. In particular both solutions exhibited a region of flow reversal detached from the mountain surface in the upstream direction. However, in numerical solutions with an upstream

inversion in the sounding, regions with no flow reversal exhibited very little variation with height below the mountain-top. This structure is similar to the RGSW model where no variations with height are present in each fluid layer. The upstream regions of non-reversed flow in the numerical solutions of constant stability soundings show significant variation with height. This result is relatively independent of the static-stability aloft.

Further testing of how well estimates of upstream soundings with inversions fit into either the CSCS parameter space or the RGSW parameter space were conducted by considering three measures of blocking. The first was the difference between the numerically computed stagnation point in the CSCS model with either the bulk or average estimate of the numerically calculated stagnation point in the solution with an upstream inversion. Between the bulk and averaging methods of the low-level stability, the averaging method did a better overall job in estimating the ϵ at which occurs stagnation in the CSCS model.

The difference between the average estimate of ϵ at stagnation in the solution with an upstream inversion and the value of ϵ at stagnation in a solution with constant stability upstream is small for all values of β and inversion heights that we tested. For example Fig. 4.6c shows that the stagnation threshold for a $\beta = 4$ mountain in the constant stability case is $\widehat{\epsilon} \approx 1.1$. If an below-mountain-top inversion is present and the bulk method is used to estimate the stability the threshold for flow stagnation is $\widehat{\epsilon}_B \approx 1.4$ where as if the average method is used the threshold is $\widehat{\epsilon}_A \approx 1.0$. If one uses the bulk method to calculate $\epsilon_B = 1.1$ and expects reversed flow they would be in serious error. The errors are even more significant for the mountain-top inversion and for mountains with smaller β.

We also considered the difference between the the analytically calculated stagnation point in the RGSW theory and the Fr, estimated from the sounding with an inversion, at the stagnation point. While the RGSW method performed well for the below-mountain-top inversion, the performance for the mountain-top inversion was

mediocre. There was a large dependence on β for the difference between the RGSW estimate of the stagnation point and the analytic prediction of the stagnation point for the mountain-top inversion. This dependence should be expected since there is no dependence on β for stagnation in the RGSW theory. There was also a large uncertainty in the difference due primarily to uncertainty in the placement of the height of the fluid interface. This is because as the upstream fluid interface approaches the height of the mountain the RGSW analytic theory predicts that $Fr \rightarrow 0$ in order for stagnation to be reached. Thus it would be difficult to apply the RGSW to determine flow stagnation if the inversion is near the mountain-top level. Even if the inversion is below-mountain-top care should be taken since there is a significant dependence on β on stagnation which is not captured by the RGSW theory.

A related measure of flow blocking that we tested was the minimum wind speed on the upstream slope. We found that, when comparing the minimum wind speed in the solution with an upstream inversion to the minimum wind speed in the solution calculated with constant upstream stability, the average method did a far better job at estimating the correct value of ϵ. In other words the difference between the averaged value of ϵ and the constant stability value of ϵ was small for identical minimum wind speeds in both the solution with an upstream inversion and the solution with constant stability.

The third measure of flow blocking we tested was the amount of low-level mass diverted laterally around the mountain. We found the bulk estimate was better than the average estimate in representing the the value of ϵ in the CSCS theory for the diverted flow. However, the bulk method only performed well when the inversion was below-mountain-top and the true value of ϵ in the CSCS theory was small. As both the bulk estimate and true value of ϵ increased the the amount of flow diversion in the solution with an inversion upstream increased more rapidly than in the case with constant stability.

Our study showed that the use of the constant-stability constant-stratification

theory of flow over topography appears to perform better than the reduced-gravity shallow-water theory when determining if the flow will be reversed on the upstream slope. There is no single technique for converting the non-uniform stability profile into a single constant value of ϵ the performs best in all our tests. On one hand, we showed that to apply the continuously-stratified, constant-stability theory a bulk estimate of the low-level stability was better than an average estimate in determining the amount of mass that deviates around the mountain. Yet on the other hand, the average method was far superior to the bulk method in determining the minimum wind speed and threshold of flow reversal in the continuously-stratified, constant-stability theory.

BIBLIOGRAPHY

Bauer, M., G. Mayer, I. Vergeiner, and H. Pichler, 2000: Strongly non-liner flow over and around a three-dimensional mountain as function of the horizontal aspect ratio. *J. Atmos. Sci.*, **57**, 3971–3991.

Bougeault, P., 1983: A non-reflective upper boundary condition for limited-height hydrostatic models. *Mon. Wea. Rev.*, **111**, 420–429.

Buzzi, A., N. Tartaglione, and P. Malguzzi, 1998: Numerical simulations of the 1994 Piedmont flood: Role of orography and moist processes. *Mon. Wea. Rev.*, **126**, 2369–2383.

Chen, Y. and J. Feng, 1995: The influences of inversion height on precipitation and airflow over the island of Hawaii. *Mon. Wea. Rev.*, **123**, 1660–1676.

Durran, D. and J. Klemp, 1983: A compressible model for the simulation of moist mountain waves. *Mon. Wea. Rev.*, **111**, 2341–2361.

Durran, D. R., 1999: *Numerical Methods for Wave Equations in Geophysical Fluid Dynamics*. Springer, 465 pp.

Epifanio, C. C. and D. R. Durran, 2001: Three-dimensional effects in high-drag-state flows over long ridges. *J. Atmos. Sci.*, **58**, 1051–1065.

Georgelin, M. and E. Richard, 1996: Numerical simulations of flow diversion around the Pyrnees: A Tranmontana case study. *Mon. Wea. Rev.*, **124**, 687–700.

Jiang, Q., 2003: Moist dynamics of orographic precipitation. *Tellus*, **55A**, 301–316.

Jiang, Q., J. D. Doyle, and R. B. Smith, 2005: Blocking, descent and gravity waves: Observations and modeling of a MAP northerly foehn event. *Quart. J. Roy. Met. Soc.*, **131**, 675–701.

Kitabayashi, K., 1977: Wind tunnel and field studies of stagnant flow upstream of a ridge. *J. Met. Soc. Japan*, **55**, 193–203.

Klemp, J. and D. R. Durran, 1983: An upper boundary condition permitting internal gravity wave radiation in numerical mesoscale models. *Mon. Wea. Rev.*, **111**, 430–444.

Lamb, V. and R. Britter, 1984: Shallow flow over an isolated obstacle. *J. Fluid Mech.*, **147**, 291–313.

LeVeque, R. J., 1996: High-resolution conservative algorithms for advection in incompressible flow. *SIAM J. Numer. Anal.*, **33**, 627–665.

Lilly, D. K., 1962: On the numerical simulation of buoyant convection. *Tellus*, **14**, 148–172.

Manins, B. L., P. C. Sawford, 1982: Mesoscale observations of upstream blocking. *Quart. J. Roy. Met. Soc.*, **108**, 427–434.

Marwitz, J. D., 1983: The kinematics of orographic airflow during Sierra storms. *J. Atmos. Sci.*, **40**, 1218–1227.

Mass, C. F. and G. K. Ferber, 1990: Surface pressure perturbations on an isolated mesoscale topographic barrier. Part I: General characteristics and dynamics. *Mon. Wea. Rev.*, **118**, 2579–2596.

Mobbs, S., S. Vosper, P. Sheridan, R. Cardoso, R. Burton, S. Arnold, M. Hill, M. Horlacher, and A. Gadian, 2005: Observations of downslope winds and rotors in the Falkland Islands. *Quart. J. Roy. Met. Soc.*, **131**, 329–351.

Ólafsson, H. and P. Bougeault, 1996: Non-linear flow past an elliptical mountain range. *J. Atmos. Sci.*, **53**, 2465–2489.

Rotunno, R. and R. Ferretti, 2001: Mechanisms of alpine rainfall. *J. Atmos. Sci.*, **58**, 1732–1749.

Schär, C. and R. B. Smith, 1993: Shallow-water flow past isolated topography, Part I: Vorticity production and wake formation. *J. Atmos. Sci.*, **50**, 1373–1400.

Schneidereit, M. and C. Schär, 2000: Idealized numerical experiments of alpine flow regimes and Southside precipitation events. *Meteor. Atmos. Phys.*, **72**, 233–250.

Smith, R., 1989: Mountain induced stagnation points in hydrostatic flow. *Tellus*, **41A**, 270–274.

Smith, R. B., 1988: Linear theory for stratified flow past an isolated mountain in isosteric coordinates. *J. Atmos. Sci.*, **45**, 3889–3896.

Smith, R. B. and S. Grønås, 1993: Stagnation points and bifurcation in 3-D mountain airflow. *Tellus*, **45A**, 28–43.

Smith, R. B. and V. Grubisic, 1993: Aerial observations of Hawaii's wake. *J. Atmos. Sci.*, **50**, 3728–3750.

Smith, R. B., S. Skubis, J. D. Doyle, A. S. Broad, C. Kiemle, and H. Volkert, 2002: Mountain waves of Mount Blanc: Influence of a stagnant boundary layer. *J. Atmos. Sci.*, **59**, 2073–2092.

Smolarkiewicz, P. and R. Rotunno, 1990: Low froude number flow past three-dimensional obstacles. Part II: Upwind flow reversal zone. *J. Atmos. Sci.*, **47**, 1498–1511.

Thorsteinsson, S. and S. Sigurdsson, 1996: Orogenic blocking and deflection of stratified air flow on anf-plane. *Tellus*, **48A**, 572–583.

Zangl, G., 2004: Upstream effects of an alpine-scale mountain ridge under various flow angles. *Meteor. Z.*, **13**, 291–296.